Multidimensional modeling of two-phase flow and heat transfer

Michael Z. Podowski
Center for Multiphase Research, Rensselaer Polytechnic Institute, Troy, New York, USA

Received 5 December 2006
Revised 4 June 2007
Accepted 4 June 2007

Abstract

Purpose – This paper seeks to discuss a mechanistic modeling concept for local phenomena governing two- and multi-phase flows and heat transfer.

Design/methodology/approach – An overview is given of selected issues concerning the formulation of multidimensional models of two-phase flow and heat transfer. A complete computational multiphase fluid dynamics (CMFD) model of two-phase flow is presented, including local constitutive models applicable to two-phase flows in heated channels. Results are shown of model testing and validation.

Findings – It has been demonstrated that the overall model is capable of capturing various local flow and heat transfer phenomena in general, and the onset of temperature excursion (CHF) in low quality forced-convection boiling, in particular.

Research limitations/implications – Whereas the multiphase model formulation is applicable to a large class of problems, geometries and operating conditions, the closure laws and results are focused on forced-convection boiling in heated channels.

Practical implications – The proposed approach can be used to predict multidimensional velocity field and phase distribution in two-phase flow devices and components used in thermal power plants, nuclear power plants and chemical processing plants.

Originality/value – A complete mechanistic multidimensional model of forced-convection boiling in heated channels is given. The potential of a CMFD approach is demonstrated to perform virtual experiments that can be used in system design and optimization, and in safety analysis.

Keywords Flow, Heat transfer, Modelling

Paper type Research paper

1. Introduction

The growing range of applications and the needs for a better understanding of multiphase phenomena in various branches of technology require analytical and computational tools that extend far beyond the current generation codes. The necessary innovations encompass modeling concepts, problem formulation and computational methods. It is interesting to note that in addition to fundamental theoretical advancements affecting the design and operation of various industrial systems, the application of new mechanistic models and codes will also have significant direct impact on cost effectiveness. This is due to the fact that computer simulations using physically-based models can contribute to reducing the experimental efforts which are needed today mainly to obtain data for new correlations being developed for specific system designs and operating conditions. Furthermore, a better understanding of the physics of multiphase flows should help to design future experiments and develop new instrumentation and experimental techniques.

The objective of this paper is to present an overview of selected issues concerning the formulation of local multidimensional models of two-phase flow and heat transfer,

International Journal of Numerical Methods for Heat & Fluid Flow
Vol. 18 No. 3/4, 2008
pp. 491-513

0961-5539
DOI 10.1108/09615530810853691

including: properly capturing the governing physical phenomena, consistency of model formulation, and specific applications and experimental validations.

2. Multifield model

2.1 Generic ensemble-averaged conservation equations

Assuming that the k-th ($k = 1, 2, \ldots$) component of the multifluid flow can be modeled using the concept of continuum, the corresponding Eulerian conservation equations for mass, momentum and energy, respectively, become:

$$\frac{\partial \rho_k}{\partial t} + \nabla \cdot (\rho_k v_k) = 0 \tag{1}$$

$$\frac{\partial (\rho_k v_k)}{\partial t} + \nabla \cdot (\rho_k v_k v_k) = -\nabla p_k + \nabla \cdot \underline{\underline{\tau}}_k + \rho_k g \tag{2}$$

$$\frac{\partial (\rho_k e_k)}{\partial t} + \nabla \cdot (\rho_k v_k e_k) = -\nabla \cdot [(-p_k \underline{\underline{I}} + \underline{\underline{\tau}}_k) \cdot v_k] - \nabla \cdot q''_k + \rho_k g \cdot v_k \tag{3}$$

For any k, these equations are valid only at locations that pertain to fluid-k at a given time instant. At the boundaries between the fluids or phases (which may vary with time), appropriate boundary conditions must be formulated, such as those for the continuity of velocity, shear stress and heat flux. Note that if the interfaces are being modeled as sharp discontinuities in fluid density and other properties, parameters such as pressure and velocity and temperature gradients, may also experience discontinuities.

The multifield modeling concept of interpenetrating fluids is based on applying the time and space, or, in general, ensemble (statistical) averaging techniques to instantaneous conservation equations for each fluid. The resultant equations are determined with respect to a common physical and computational domain, and include terms accounting for the various interfacial effects between the individual fields.

A typical form of conservation equations for mass, momentum and energy, respectively, obtained by applying the appropriate averaging procedure to equations (1)-(3), respectively, can be written as:

$$\frac{\partial (\alpha_k \rho_k)}{\partial t} + \nabla \cdot (\alpha_k \rho_k \bar{v}_k) = \Gamma_k \tag{4}$$

$$\frac{\partial (\alpha_k \rho_k \bar{v}_k)}{\partial t} + \nabla \cdot (\alpha_k \rho_k \bar{v}_k \bar{v}_k) = -\nabla (\alpha_k \bar{p}_k) + \nabla \cdot \left(\alpha_k \underline{\underline{\bar{\tau}}}{}^t_k \right) + \alpha_k \rho_k g + \tilde{M}^i_k \tag{5}$$

$$\begin{aligned} \frac{\partial (\alpha_k \rho_k \bar{e}_k)}{\partial t} + \nabla \cdot (\alpha_k \rho_k \bar{v}_k \bar{e}_k) = -\nabla \cdot \left(\alpha_k \bar{q}''^t_k \right) - \nabla \cdot \left[\alpha_k \left(-\bar{p}_k \underline{\underline{I}} + \underline{\underline{\bar{\tau}}}{}^t_k \right) \cdot \bar{v}_k \right] \\ + \alpha_k \rho_k g \cdot \bar{v}_k + E^i_k \end{aligned} \tag{6}$$

where $\underline{\underline{\bar{\tau}}}{}^t_k = \underline{\underline{\bar{\tau}}}{}^\mu_k + \underline{\underline{\bar{\tau}}}{}^{\mathrm{Re}}_k$ is the total combined shear and turbulent shear stress, $\bar{q}''^t_k = \bar{q}''^k_k + \bar{q}''^{\mathrm{Re}}_k$ is the total heat flux, and the corresponding interfacial source terms for fluid-k are given by:

$$\Gamma_k = -\frac{1}{\Delta t} \sum_{i \in [\Delta t]} \frac{1}{\left| v^i_k \cdot n_k \right|} \rho_k \left(v_k - v^i_k \right) \cdot n_k \tag{7}$$

$$\tilde{M}^i_k = -\frac{1}{\Delta t}\sum_{i\in[\Delta t]}\frac{1}{\left|v^i_k\cdot n_k\right|}\left[\rho_k v_k\left(v_k - v^i_k\right) + p_k I - \underline{\underline{\tau}}^t_k\right]\cdot n_k \tag{8}$$

$$E^i_k = -\frac{1}{\Delta t}\sum_{i\in[\Delta t]}\frac{1}{\left|v^i_k\cdot n_k\right|}\left[\rho_k e_k\left(v_k - v^i_k\right) + p_k I - q''^t_k\right]\cdot n_k \tag{9}$$

2.2 Effect of interactions between fields representing same phase

The model given by equations (4)-(6) has been derived for gas-liquid two-phase flows with well defined topology. Specifically, it applies to dispersed bubbly flows where the interfacial interactions occur across bubble/liquid interfaces that gradually evolve in time and space. However, in the case where the interfacial interactions occur within a given phase, e.g. between dispersed liquid droplets and a liquid film, or as a result of bubble coalescence or breakup, the ensemble-averaged conservation equations, equations (4)-(6), must be complemented with additional terms. This, in turn, leads to the formulation of a general multifield model of multiphase flows. In this model, which is a generalization of the well-established two-fluid model, the individual fields may represent either separate fluids and phases, or geometrically/topologically distinct flow configurations within a given physical fluid or phase (e.g. continuous liquid field, dispersed small bubbles or particles, large deformed bubbles or bubble clusters, continuous gas/vapor field, and dispersed liquid field – droplets). In such model, the interfacial source terms in equations (4)-(6), respectively, must be expanded by adding the appropriate interfacial transfer terms associated with the interfacial mass transfer from field-*n* into field-*k*, $m'''_{m,k}$, both representing the same phase. The mass, momentum and energy, respectively, conservation equations for a multifield model of gas/liquid flow can be written as:

$$\frac{\partial(\alpha_k\rho_k)}{\partial t} + \nabla\cdot(\alpha_k\rho_k\bar{v}_k) = \Gamma_k + m'''_k \tag{10}$$

$$\begin{aligned}\frac{\partial(\alpha_k\rho_k\bar{v}_k)}{\partial t} + \nabla\cdot(\alpha_k\rho_k\bar{v}_k\bar{v}_k) = {} & -\alpha_k\nabla\bar{p}_k - \sum_j\left(\bar{p}_k - p^i_{kj}\right)\nabla\alpha_k + \alpha_k\nabla\cdot\underline{\underline{\bar{\tau}}}^t_k \\ & + \sum_j\left(\underline{\underline{\bar{\tau}}}^t_k - \underline{\underline{\tau}}^i_{kj}\right)\nabla\alpha_k + \sum_j M^i_{kj} + \alpha_k\rho_k g \\ & + \sum_n\Gamma_{n,k}v^i_n + \sum_m m'''_{m,k}v^i_m\end{aligned} \tag{11}$$

$$\begin{aligned}\frac{\partial(\alpha_k\rho_k\bar{e}_k)}{\partial t} + \nabla\cdot(\alpha_k\rho_k\bar{v}_k\bar{e}_k) = {} & -\nabla\cdot\left[\alpha_k\left(-\bar{p}_k\underline{\underline{I}} + \underline{\underline{\bar{\tau}}}^t_k\right)\cdot\bar{v}_k\right] - \alpha_k\nabla\cdot\bar{q}''^t_k \\ & - \sum_j\left(\bar{q}''^t_k - q''^i_{k,j}\right)\cdot\nabla\alpha_k + \alpha_k\rho_k g\cdot\bar{v}_k \\ & + \sum_n\Gamma_{n,k}e^i_{n,k} + \sum_m m'''_{m,k}e^i_{m,k}\end{aligned} \tag{12}$$

where $\Gamma_k = \sum_n\Gamma_{nk}$ and $m'''_k = \sum_m m'''_{m,k}$.

For a typical two-phase two-field model the index, *k*, includes: cl – continuous liquid phase, and dv – dispersed vapor phase. On the other hand, for a four-field model, the following fields can be used: continuous liquid phase (cl), dispersed liquid (dl), continuous vapor (cv) and dispersed vapor (dv).

Several additional conditions, or closure laws, are needed to close the model given by equations (10)-(12). The form of individual interfacial closure laws depends on the specific physical phenomena. For example, for dispersed (with small size "particles") flows, the total interfacial force is given as a superposition of terms describing various effects (Anglart *et al.*, 1977; Drew and Passman, 1999). The range of applications (limitations) and accuracy of predictions of the multifield model strongly depend on the degree to which the closure laws, determined in terms of ensemble-averaged state variables (i.e. component concentrations, velocities, specific energies, and pressures), are capable of capturing the most important (for a given situation) local mass, momentum and heat transfer phenomena. Selected issues arising from the multifield model formulation are discussed in the next section.

2.3 Governing equations for dispersed two-phase flows

Although the multifield conservation equations seem to be a direct extension of those governing single-phase flows, it turns out that the averaging procedure introduces several constraints on the formulation of individual models. One such constraint, arising from the multifield modeling concept, imposes a shear-stress coupling effect between the continuous and disperse fields.

Let us consider a two-phase flow of densely packed "particles" (bubbles, droplets or solid particles) in a continuous fluid, shown in Figure 1(a).

Ignoring phase change, a standard form of the momentum conservation equations for the dispersed and continuous fields is:

$$\begin{aligned}\frac{\partial(\alpha_d\rho_d\bar{v}_d)}{\partial t}+\nabla\cdot(\alpha_d\rho_d\bar{v}_d\bar{v}_d) &= -\alpha_d\nabla\bar{p}_d-\left(\bar{p}_d-p_d^i\right)\nabla\alpha_d+\alpha_d\nabla\cdot\bar{\underline{\underline{\tau}}}_d^t\\ &\quad+\left(\bar{\underline{\underline{\tau}}}_d^t-\underline{\underline{\tau}}_d^i\right)\cdot\nabla\alpha_d+\alpha_d\rho_d g+M_d^i\end{aligned}\tag{13}$$

$$\begin{aligned}\frac{\partial[\alpha_c\rho_c\bar{v}_c]}{\partial t}+\nabla\cdot(\alpha_c\rho_c\bar{v}_c\bar{v}_c) &= -\alpha_c\nabla\bar{p}_c-\left(\bar{p}_c-p_c^i\right)\nabla\alpha_c+\alpha_c\nabla\cdot\bar{\underline{\underline{\tau}}}_c^t\\ &\quad+\left(\bar{\underline{\underline{\tau}}}_c^t-\underline{\underline{\tau}}_c^i\right)\cdot\nabla\alpha_c+\alpha_c\rho_c g+M_c^i\end{aligned}\tag{14}$$

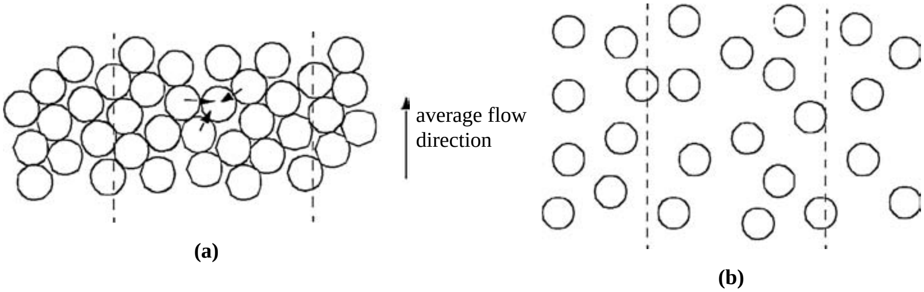

(a)

(b)

Figure 1.
Particulate two-phase flow: (a) packed particles; (b) dilute particles

Now, let us consider a two-phase flow of diluted particles dispersed in a continuous fluid, shown in Figure 1(b). Since, particles are in no contact with one another, particle motion is governed by the combination of interfacial and gravity forces. Thus, using the Lagrangian frame of reference, we write:

$$\rho_p \frac{\mathrm{d}v_p}{\mathrm{d}t} = \rho_p V_p g - F_{c-p} \tag{15}$$

Ensemble-averaging equation (15) yields:

$$\frac{\partial(\alpha_d \rho_d \bar{v}_d)}{\partial t} + \nabla \cdot (\alpha_d \rho_d \bar{v}_d \bar{v}_d) = p_d^i \nabla \alpha_d - \underline{\underline{\tau}}_d^i \cdot \nabla \alpha_d + \alpha_d(\rho_d - \rho_m) g + M_d^i \tag{16}$$

where $\rho_m = \alpha_c \rho_c + \alpha_d \rho_d$ is the mixture density.

In such case, there is no pressure force between the particles or shear-stress term in the dispersed field momentum equation. If the standard form of equation (13) is used for dilute particle flows, the results may become unphysical.

It turns out, however, that a complete two-fluid model can still be applied to such conditions, provided the dispersed field pressure (which is not an independent variable) and the continuous-field-induced shear stress on dispersed particles are properly determined based on first-principle physical considerations (Podowski, 2007). Specifically, the following relationships must be satisfied simultaneously:

$$\bar{p}_d = \bar{p}_c = \bar{p}, \quad \bar{\underline{\underline{\tau}}}_d^t = \bar{\underline{\underline{\tau}}}_c^t = \bar{\underline{\underline{\tau}}}^t \tag{17}$$

To illustrate this modeling inconsistency, simulations were performed using the NPHASE (Antal *et al.*, 2000) code for fully-developed dilute particulate flow in a horizontal tube. The effect of using equation (13) is shown in Figure 2, where the calculated particle velocity is considerably higher than the velocity of the liquid that drives the particles. This is clearly unphysical. When equation (13) was used instead (obtained by substituting equation (17) into (13)), the fully-developed velocity of particles matched the velocity field of the liquid, as expected.

3. Mechanistic predictions of forced-convection boiling heat transfer

3.1 Subcooled nucleate boiling

In the nucleate subcooled boiling in a heated channel, the wall heat is partially used to form bubbles and the remaining portion is transferred to the liquid. The heat transfer

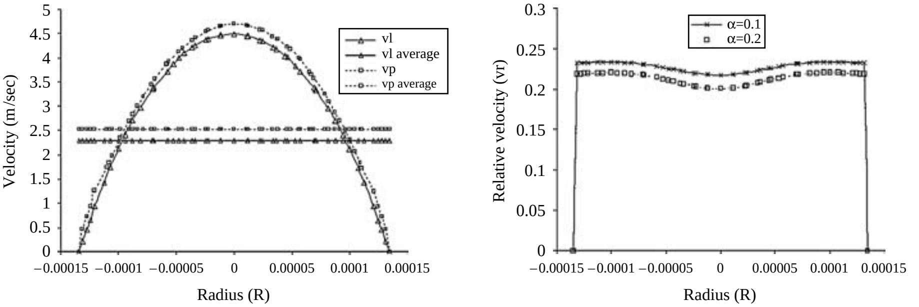

Source: Tiwari *et al.* (2003)

Figure 2. Radial profiles of: liquid (v_l), dilute particles (v_p), and relative velocity ($v_r = v_p - v_l$), across a horizontal pipe using inconsistent two-field model

from the wall in the vicinity of a nucleation site occurs during two distinct periods: the bubble growth time and the waiting time. The total convective heat flux from the wall is the sum of three component terms (Kurul and Podowski, 1991):

$$q''_{NB} = q''_{1\phi} + q''_e + q''_Q \tag{18}$$

where $q''_{1\phi}$ is the single-phase convective heat flux, q''_e is the heat flux associated with phase change (evaporation), and q''_Q is the so-called quenching heat flux, which is transferred to the liquid phase during the waiting time (Figure 3).

Outside of the influence area of the bubbles, the heat transfer from wall to the liquid can be calculated by:

$$q''_{1\phi} = A''_{1\phi} C_h \rho_l c_{pl} u_l (T_w - T_l) = H_{1\phi}(T_w - T_l) \tag{19}$$

where $A''_{1\phi}$ is the fraction of the wall unaffected by the nucleation sites, C_h is the Stanton number determined in terms of the local near-wall liquid velocity and Prandtl number, T_w is the wall temperature and T_l is the local liquid temperature near the heated wall.

The evaporation heat flux is given by:

$$q''_e = \frac{\pi}{6} d^2_{\mathrm{bw}} \rho_v f n'' h_{\mathrm{fg}} \tag{20}$$

where d_{bw} is the bubble diameter at detachment, f is the frequency of nucleation, and n'' is the number of nucleation sites per unit area (nucleation site density).

The quenching heat flux has been analytically calculated by Del Valle and Koening (1985) as:

$$q''_Q = \tau_w f A''_{2\phi} \frac{2k_l(T_w - T_l)}{\sqrt{\pi \tau_w k_l / \rho_l c_{pl}}} \tag{21}$$

where τ_w is the waiting time elapsed between the detachment of a given bubble and the nucleation of a subsequent one. The term, $A''_{2\phi}$, is the fraction of the wall area participating in the quenching heat flux.

In order to close the present model, additional relationships are needed regarding parameters such as: nucleation frequency, nucleations site density, bubble diameter at departure, etc. In particular, the nucleation frequency, f, plays a very important role in the overall analysis. Whereas various phenomenological models and correlations are available in the literature for the nucleation frequency (Ceumern-Lindenstjerna, 1977), this parameter can be also deduced from theoretical considerations of the bubble ebullition cycle.

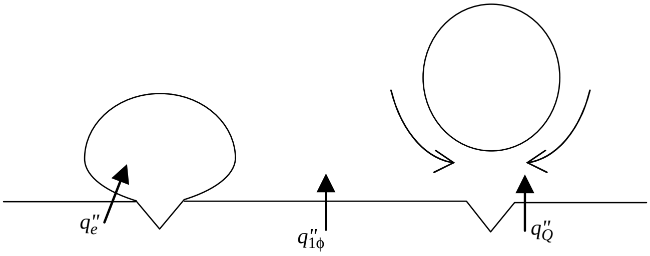

Figure 3.
Vapor structures close to the heated wall in the subcooled flow boiling

The approach combines transient heat transfer solutions for the heated wall and for the liquid laminar sublayer filling the space vacated by departing bubbles in forced convection subcooled boiling (Podowski, R.M. *et al.*, 1997). Whereas wall heat conduction is, in general, multidimensional in nature, a one-dimensional model should still be appropriate for this purpose. This is due to the fact that the characteristic time of surface temperature fluctuations during nucleation is very short, so that the distance across the wall affected by a change in the surface temperature is small compared to the size of the surface area exposed to quenching by cold water.

Using a time-dependent wall surface temperature (yet to be determined), as a boundary condition, the heat conduction equation can be solved for the time- and position-dependent temperature distribution across the wall during the inside-cavity nucleation period:

$$\hat{T}_w(y,t) = \frac{a_w}{2\sqrt{\pi}} \int_0^t [T_i(t') - T_0] \frac{y}{[a_w(t-t')]^{3/2}} \mathrm{Exp}\left[-\frac{y^2}{4a_w(t-t')}\right] \mathrm{d}t' \tag{22}$$

where T_0 is the reference steady state surface temperature prior to the onset of a new ebullition cycle, and a_w is the thermal diffusivity of the wall. For most practical applications it can be assumed that $T_0 \approx T_{\text{sat}}$.

Solving the heat conduction again for the liquid in the near-wall region and coupling the two solutions with the appropriate boundary conditions, yields the following equation for the time-dependent surface temperature during the dwell time:

$$\Re \int_0^t \frac{\mathrm{d}T_i(t')}{\mathrm{d}t'} \frac{\mathrm{d}t'}{\sqrt{t-t'}} = k_w B \tag{23}$$

where $B = -q''_{w,s}/k_w$, and $q''_{w,s} < 0$ is the steady state (average) wall heat flux, and:

$$\Re = \frac{k_w}{\sqrt{\pi a_w}} + \frac{k_l}{\sqrt{\pi a_l}} \tag{24}$$

Solving equation (23) yields (Figure 4):

$$T_i(t) = T_i(0^+) = \frac{2k_w B}{\pi \Re} \sqrt{t} \tag{25}$$

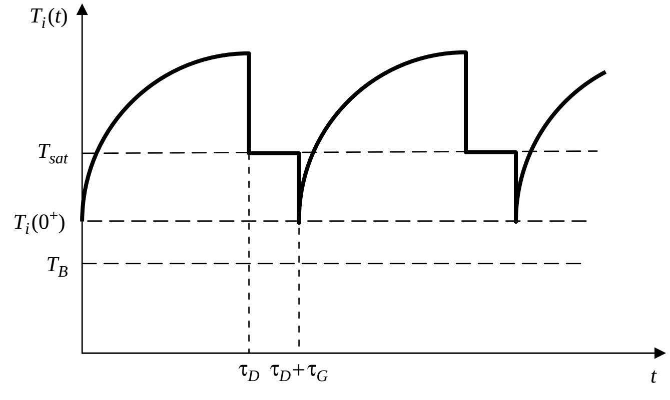

Figure 4.
Surface temperature oscillations in the wall during the ebullition cycle

Also, the time-dependent local surface heat flux can be evaluated as:

$$T_i(t) = -\frac{k_l[T_i(0^+) - T_B]}{\sqrt{\pi a_l t}} - \frac{k_l k_w B}{\Re\sqrt{\pi a_l}} \tag{26}$$

where:

$$T_i(0^+) = \left(\frac{k_w T_0}{\sqrt{a_w}} + \frac{k_l T_B}{\sqrt{a_l}}\right)\left(\frac{k_w}{\sqrt{a_w}} + \frac{k_l}{\sqrt{a_l}}\right)^{-1} \tag{27}$$

3.1.1 Solution for dwell time, τ_D. Dwell time is the period of time beginning at the moment of bubble departure and ending at the moment when the bubble radius reaches the wall cavity radius. At this point, the bubble will enter the growth period. Using equation (25), the following equation can be derived:

$$\frac{2k_w B}{\pi\Re}\sqrt{\tau_D} - \frac{[T_i(0^+) - T_B]r_c}{\sqrt{\pi a_l \tau_D}} + [T_i(0^+) - T_{\mathrm{sat}}] - \frac{Bk_w r_c}{\Re\sqrt{\pi a_l}} - \frac{2\sigma}{r_c}\frac{T_{\mathrm{sat}} v_{\mathrm{fg}}}{h_{\mathrm{fg}}} = 0 \tag{28}$$

where r_c is the cavity radius. As can be seen, for given: pressure, liquid bulk temperature, wall heat flux, cavity size, and the material properties of both the wall and the fluid, equation (28) yields an analytical expression for the bubble dwell time, τ_D.

3.1.2 Solution for growth time, τ_G. During bubble growth, the local instantaneous heat flux from the wall to the bubble is almost entirely used to evaporate the liquid sublayer between the wall and the bubble, and the resultant vapor accumulates in the growing bubble. Since, the temperature drop across the thin sublayer is very small, the local surface temperature during this period remains close to the saturation temperature (thus, $T_0 \approx T_{\mathrm{sat}}$, as shown in Figure 4). Using the corresponding energy balance with an analytically derived time-dependent surface heat flux during that period, the following relationship can be obtained between the growth time, τ_{G}, and the critical bubble diameter, $d_{b,\mathrm{crit}}$:

$$\frac{d_{b,\mathrm{crit}}\rho_g h_{\mathrm{fg}}}{2k_w} = -B\tau_G + \frac{2[T_{\mathrm{sat}} - T_i(\tau_G)]r_c}{\sqrt{\pi a_w}}\sqrt{\tau_G} \tag{29}$$

Several different models have been developed to evaluate the bubble diameter at departure. A simple model was proposed by Tolubinsky and Kostanchuk (1970), whereas another, more mechnistic (based on the force balance for a single bubble) model was developed by Staub (1968).

Finally, the total bubble departure time and the frequency of bubble departure from a cavity can be obtained from:

$$f_{\mathrm{dep}} = \frac{1}{\tau_{\mathrm{dep}}} = \frac{1}{\tau_D + \tau_G} \tag{30}$$

Another closure law, for the nucleation site density in equation (20) is obtained from the experimental data of Lemmert and Chawla (1977):

$$n'' = [m(T_w - T_l)]^{1.805} \quad \text{where } m = 185 \tag{31}$$

modified to account for the fact that even when the two neighboring nucleation sites are very close to each other, they may still be active if they are nucleating out of phase and if the waiting time is long enough. Details are given by Kurul and Podowski (1990, 1991) and Podowski (2000).

In addition to the near wall phenomena, it is important that the local interfacial heat transfer between the bubbles departing from the heated wall and the liquid be accounted for in the overall multidimensional model. In particular, the interfacial heat flux can be determined from:

$$q_i'' = \frac{k_c}{D_H}\left[2 + 0.6\left(\frac{\rho_l d_b |v_r|}{\mu_l}\right)^{0.5} \mathrm{Pr}_l^{0.33}\right] A_b'''(T_{\mathrm{sat}} - T_l) \tag{32}$$

where A_b''' is the vapor interfacial area density and v_r is the gas-to-liquid relative velocity.

Since, the vapor temperature is close to the saturation temperature, the interfacial phase change (condensation) rate can be obtained from, $\Gamma_c = q_i'''/h_{\mathrm{fg}}$.

The models described above have been tested and validated against experimental data. In particular, the heat flux partitioning model was incorporated in the CFX (AEA, 1998) computer code and used to predict temperature and void fraction distribution for various experimental data sets. An example showing the results of simulations for the experiments of Velidandla *et al.* (1995) in an annular channel heated for inside are shown in Figure 5. As it can be seen, the agreement between the predicted and measured radial void distribution is excellent.

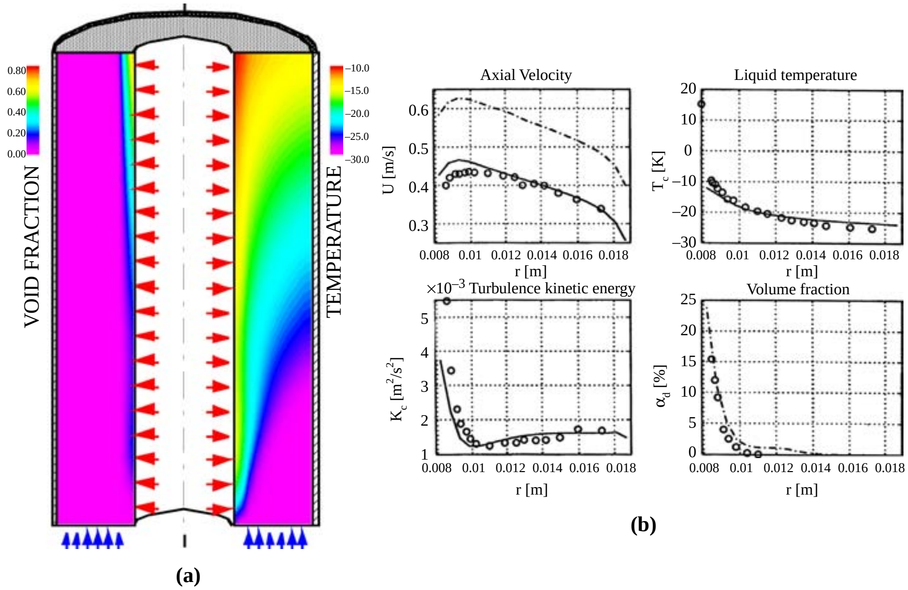

Notes: (a) Local void and temperature distributions along the channel; (b) comparison between calculations and data for radial distributions of major parameters at channel exit

Sources: Kurul *et al.* (1996) and Alajbegovic *et al.* (1996)

Figure 5.
Predicted and measured local hydrodynamic and thermal parameters for subcooled boiling in an annular channel heated from inside

3.2 Critical heat flux and temperature excursion

The physical fundamentals of the model discussed in this section are based on the extensive experimental evidence concerning local phenomena and flow structure near the heated wall, such as: the bubble-ebullition process (i.e. bubble formation, growth, detachment from the nucleation site, departure from the wall, and collapse), the velocity, phase and temperature distributions, and the conditions which may lead to wall temperature excursion (CHF). The processes of bubble formation, its growth/collapse, and flow structure conditions leading to CHF are shown in Figure 6 and can be classified as (Alajbegovic *et al.*, 1997; Podowski, M.Z. *et al.*, 1997):

- bubble formation and initial growth inside the superheated thermal sublayer (due to condensation in contact with subcooled liquid, bubbles can reach their maximum size either while still attached to the heated wall or after they depart from the surface);
- at high-heating rates, small bubbles start coalescing near the wall and form larger elongated bubbles; and
- nucleation of small bubbles continues to occur between the elongated bubbles, as long as liquid replenishment at the surface is possible.

The formation of elongated bubble formation is shown in Figure 6.

In the presence of elongated bubbles, the average wall heat flux can partitioned into the following terms:

$$\bar{q}''_w = \bar{q}''_{\mathrm{sb}} + \bar{q}''_{\mathrm{lb}} = q''_H \tag{33}$$

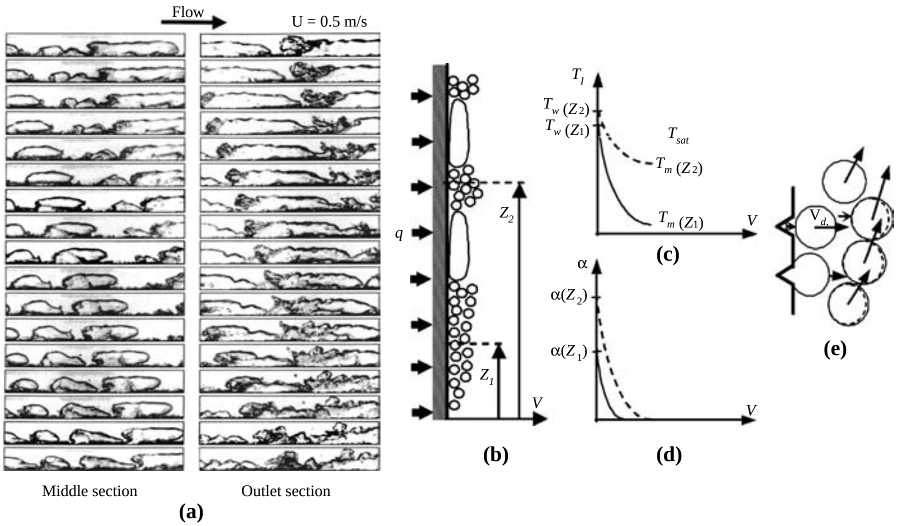

Figure 6.
Flow neat the heated wall in low-quality flow boiling

Notes: (a) Experimental observations Galloway and Moudawar (1993) of elongated bubble formation; (b) a schematic of the near-wall bubble structure; (c) near-wall temperature distribution; (d) near-wall void fraction distribution; (e) nucleation-induced force pushing bubbles away from the heated wall

Reproduced from the only available original where $\bar{q}''_{\mathrm{sb}}$ is the component of the total wall heat flux corresponding to the dispersed bubble region (Section 3.1), $\bar{q}''_{\mathrm{lb}}$ is the component associated with heat transfer between the wall and the elongated bubbles, and q''_H is the average heated power per unit surface area:

$$q''_H = \frac{q_H}{A_H} \tag{34}$$

The fractional wall heat flux pertaining to the dispersed bubble region can be determined from:

$$\bar{q}''_{\mathrm{sb}} = \bar{q}''_{\mathrm{NB}} A''_{\mathrm{NB}} \tag{35}$$

where $\bar{q}''_{\mathrm{NB}}$ is the nucleate boiling heat flux given by equation (18) and A''_{NB} is the heated surface area fraction (area density) in the dispersed bubble region (Figure 7).

In general, the continuous vapor heat flux can be written as a sum of two terms:

$$\bar{q}''_{\mathrm{lb}} = \bar{q}''_{\mathrm{LS}} A''_{\mathrm{LB}} \frac{L_{\mathrm{LS}}}{L_{\mathrm{LB}}} + \bar{q}''_{\mathrm{dry}} A''_{\mathrm{LB}} \left(1 - \frac{L_{\mathrm{LS}}}{L_{\mathrm{LB}}}\right) \tag{36}$$

where A''_{LB} is the area density for the elongated bubbles, $\bar{q}''_{\mathrm{LS}}$ is the heat flux across the liquid sublayer, $\bar{q}''_{\mathrm{dry}}$ is the heat flux in the dry region of elongated bubbles, L_{LB} is the length of elongated bubbles and L_{LS} is the length of the liquid sublayer region between the elongated bubble and the wall.

It should be noted that, depending on the flow and heat transfer conditions near the heated wall, the liquid sublayer separating elongated bubbles from the wall may extend along the entire length of the bubble, or, if the evaporation rate is sufficiently high, a dry region may form bringing a portion of the bubble area to direct contact with the wall (Figure 7).

The measurements of the length of large bubbles (Galloway and Mudawar, 1993; Gersey and Mudawar, 1995) show that it agrees well with the critical wavelength of the Helmholtz instability at the vapor/liquid interface. Comparing the pressure drop at the wavy interface calculated from the kinematic considerations to that due to surface tension yields the following expression for the critical length of a large bubble:

$$L_{\mathrm{LB}} = \frac{2\pi\sigma(\rho_f + \rho_g)}{\rho_f \rho_g (u_{\mathrm{LB}} - u_l)^2} \tag{37}$$

where u_{LB} is the elongated bubble velocity, and u_{l} is the local liquid velocity around the bubble.

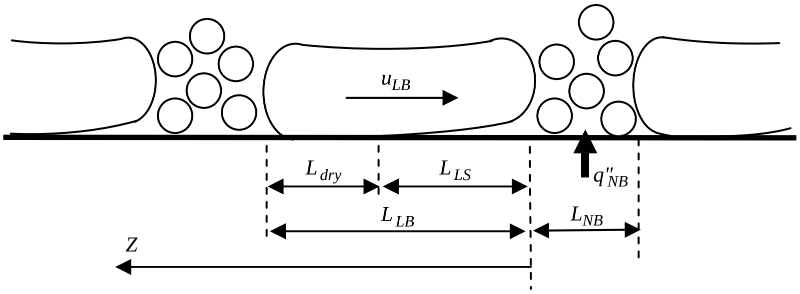

Figure 7.
Phase distribution in the near-wall region

Another parameter of interest to the present model is the distance between the elongated bubbles and the wall. As stated before, these bubbles flow very close to the walls, at an initial distance (i.e. at the tip of the bubbles) corresponding to the viscous sublayer thickness. Thus, the initial distance between the bubbles and the wall can be evaluated (Alajbegovic *et al.*, 1997) as, $\delta_0 = 10v/u_\tau$, where $u_\tau = \sqrt{\tau_w/\rho_l}$ is the shear velocity.

3.2.1 Case (A). Let us first consider the situation where the liquid sublayer extends over the entire length of elongated bubbles (i.e. there is no dry region). In such case, equation (36) becomes:

$$\bar{q}''_{\mathrm{lb}} = \bar{q}''_{\mathrm{LB}} A''_{\mathrm{LB}} \tag{38}$$

As long as the heated wall is relatively thin, i.e. $\mathrm{Bi} = H\delta_w/k_w \leq 0.1$, where δ_w and k_w are the wall thickness and thermal conductivity, respectively, and H is the heat transfer coefficient across the liquid sublayer, the local wall temperature can be obtained from a 1-D heat conduction equation:

$$\rho_w c_{\mathrm{pw}} \delta_w \frac{\partial T_w}{\partial t} = \rho_w c_{\mathrm{pw}} \delta_w u_{\mathrm{LB}} \frac{\mathrm{d}T_w}{\mathrm{d}z} = q''_H - q''_s + \delta_w k_w \frac{\mathrm{d}^2 T_w}{\mathrm{d}z^2} \tag{39}$$

where the independent variable, z, is moving with the elongated bubble (Figure 7).

Furthermore, it can be shown that for a thin heater wall, the axial conduction term rate can be neglected. Thus, equation (39) simplifies to:

$$\rho_w c_{\mathrm{pw}} \delta_w u_{\mathrm{LB}} \frac{\mathrm{d}T_w}{\mathrm{d}z} \approx q''_H - q''_s \tag{40}$$

In the wall region along a single elongated bubble separated from the wall by a liquid sublayer, the wall heat flux is given by:

$$q''_s = q''_{\mathrm{LB}} = \frac{k_l}{\delta_{\mathrm{LS}}}(T_w - T_{\mathrm{sat}}) \tag{41}$$

Consequently, equation (40) becomes:

$$\rho_w c_{\mathrm{pw}} \delta_w u_{\mathrm{LB}} \frac{\mathrm{d}T_w}{\mathrm{d}z} = q''_H - \frac{k_l}{\delta_{\mathrm{LS}}}(T_w - T_{\mathrm{sat}}) \tag{42}$$

where the liquid sublayer thickness satisfies the energy conservation equation:

$$\rho_w h_{\mathrm{fg}} u_{\mathrm{LB}} \frac{\mathrm{d}\delta_{\mathrm{LS}}}{\mathrm{d}z} = -q''_{\mathrm{LB}} = -\frac{k_l}{\delta_{\mathrm{LS}}}(T_w - T_{\mathrm{sat}}) \tag{43}$$

Equations (42) and (43) can be rewritten as:

$$\frac{\mathrm{d}\theta_w}{\mathrm{d}z} = a_1 - b_1 \frac{\theta_w}{\delta_{\mathrm{LS}}} \tag{44}$$

$$\frac{\mathrm{d}\delta_{\mathrm{LS}}}{\mathrm{d}z} = -c \frac{\theta_w}{\delta_{\mathrm{LS}}} \tag{45}$$

where $\theta_w = T_w - T_{\mathrm{sat}}$, $a_1 = q''_H/\rho_w c_{\mathrm{pw}} \delta_w u_{\mathrm{LB}}$, $b_1 = k_l/\rho_w c_{\mathrm{pw}} \delta_w u_{\mathrm{LB}}$ and $c = k_l/\rho_w c_{\mathrm{pw}} h_{\mathrm{fg}}$.

Using the following boundary conditions:

$$\theta_w(0) = \theta_{w,o} \tag{46}$$

$$\delta_{\mathrm{LS}}(0) = \delta_{\mathrm{LS},o} \tag{47}$$

Equations (44) and (45) can be solved analytically, to obtain the following algebraic equation for:

$$\begin{aligned}&\ln\frac{c\phi^2(z) - b_1\phi(z) + a_1}{c\phi_o^2 - b_1\phi_o + a_1} + \frac{b_1}{\sqrt{4a_1c - b_1^2}}\left[a\tan\frac{2c\phi(z) - b_1}{\sqrt{4a_1c - b_1^2}} - a\tan\frac{2c\phi_o - b_1}{\sqrt{4a_1c - b_1^2}}\right] \\ &= \ln\left[\frac{\phi(z) - (b_1/c)}{(a_1/\delta_{\mathrm{LS},o})z + (\phi_o - (b_1/c))}\right]^2\end{aligned} \tag{48}$$

where:

$$\phi(z) = \frac{\theta_w(z)}{\delta_{\mathrm{LS},o} + c/b_1\left[\theta_w(z) - \theta_{w,o} + a_1 z\right]}, \quad \phi_o = \frac{\theta_{w,o}}{\delta_{\mathrm{LS},o}} \tag{49}$$

Also, the position-dependent thickness of the liquid sublayer can be obtained from:

$$\delta_{\mathrm{LS}}(z) = \delta_{\mathrm{LS},o} + \frac{c}{b_1}\left[\theta_w(z) - \theta_{w,o} + a_1 z\right] \tag{50}$$

As can be seen, for given $\theta_{w,o}$, $\delta_{\mathrm{LS},o}$ and L_{LB}, equations (48) and (50) can be used to determine the wall temperature at the end of the section adjacent to the elongated bubble, $\theta_w(L_{\mathrm{LB}}) = \theta_{w,1}$.

For the nucleate boiling region, we write:

$$\rho_w c_{pw}\delta_w u_{\mathrm{LB}}\frac{\mathrm{d}T_w}{\mathrm{d}z} = q''_H - q''_{\mathrm{NB}} \tag{51}$$

where:

$$q''_{\mathrm{NB}} = (b_Q + H_{1\phi})(T_{\mathrm{sat}} - T_l) + b_e(T_w - T_{\mathrm{sat}})^{1.805} + H_{1\phi}(T_w - T_{\mathrm{sat}}) \tag{52}$$

Equation (51) can be rewritten as:

$$\frac{\mathrm{d}\theta_w}{\mathrm{d}z} \approx a_2 - b_{21}\theta_w - b_{22}\theta_w^2 \tag{53}$$

where:

$$a_2 = \frac{q''_H - (b_Q + H_{1\phi})(T_{\mathrm{sat}} - T_l)}{\rho_w c_{\mathrm{pw}}\delta_w u_{\mathrm{LB}}}, \quad b_{21} = \frac{H_{1\phi}}{\rho_w c_{\mathrm{pw}}\delta_w u_{\mathrm{LB}}}, \quad b_{22} = \frac{b_e(T_{w,o} - T_{\mathrm{sat}})^{-0.192}}{\rho_w c_{\mathrm{pw}}\delta_w u_{\mathrm{LB}}}.$$

Using the boundary condition:

$$\theta_w(L_{\mathrm{LB}}) = \theta_{w,1} \tag{54}$$

the solution of equation (53) is:

$$\frac{\theta_w(z) - \vartheta_1}{\theta_w(z) - \vartheta_2} = \frac{\theta_{w,1} - \vartheta_1}{\theta_{w,1} - \vartheta_2}\,\mathrm{Exp}\,[-b_{22}(\vartheta_1 - \vartheta_2)(z - L_{\mathrm{LB}})] \tag{55}$$

where:

$$\vartheta_1 = -\frac{b_{21}}{2b_{22}} + \sqrt{\frac{b_{21}^2}{4b_{22}^2} + \frac{a_2}{b_{22}}} \text{ and } \vartheta_2 = -\frac{b_{21}}{2b_{22}} - \sqrt{\frac{b_{21}^2}{4b_{22}^2} + \frac{a_2}{b_{22}}}.$$

Noting that for a quasi-periodic wall temperature distribution (corresponding to an almost constant average wall temperature over the elongated bubble length scale) we have:

$$\theta_w(L_{\mathrm{LB}} + L_{\mathrm{NB}}) = \theta_{w,o} \tag{56}$$

it can be readily seen that, for a given $\delta_{\mathrm{LS,o}}$, the combined equations (48) and (49) and equations (54)-(56) can be solved for $\theta_{w,0}$ and $\theta_{w,1}$. Substituting the calculated values back into equations (48) and (49) and equation (55), the wall temperature distribution along each subregion can be determined. Subsequently, the average wall heat fluxes in the liquid sublayer (long bubble) and nucleate boiling regions, respectively, can be obtained from:

$$\bar{q}''_{\mathrm{LB}} = \frac{k_l}{L_{\mathrm{LB}}}\int_0^{L_{\mathrm{LB}}} \frac{\theta_w(z)}{\delta_{\mathrm{LS}}(z)}\,\mathrm{d}z \tag{57}$$

$$\bar{q}''_{\mathrm{NB}} = \frac{1}{L_{\mathrm{NB}}}\int_{L_{\mathrm{LB}}}^{L_{\mathrm{LB}}+L_{\mathrm{NB}}} \{(b_Q + H_{1\phi})(T_{\mathrm{sat}} - T_l) + b_e[\theta_w(z)]^{1.805} + H_{1\phi}\theta_w(z)\}\,\mathrm{d}z \tag{58}$$

where $\delta_{\mathrm{LS}}(z)$ is given by equation (50).

Also, the average wall temperature can be obtained from:

$$\bar{\theta}_w = \frac{1}{L_{\mathrm{LB}} + L_{\mathrm{NB}}}\int_0^{L_{\mathrm{LB}}+L_{\mathrm{NB}}} \theta_w(z)\,\mathrm{d}z \tag{59}$$

3.2.2 Case (B). In this case, the liquid sublayer evaporates completely over a distance smaller than the length of the elongated bubble. For the region corresponding to the liquid sublayer, we can still use equations (44) and (45). Denoting, $\theta_w(L_{\mathrm{LS}}) = \theta_{w,1}$, we obtain:

$$\ln\left[\frac{(\theta_{w,1}/\delta_{\mathrm{LS},o})^2}{\phi_o^2 - (b_1/c)\phi_o + (a_1/c)}\right] + \frac{b_1}{\sqrt{4a_1c - b_1^2}}\left[\frac{\pi}{2} - a\tan\frac{2c\phi_o - b_1}{\sqrt{4a_1c - b_1^2}}\right] = 0 \tag{60}$$

and:

$$\delta_{\mathrm{LS},o} + \frac{c}{b_1}\left[\theta_{w,1} - \theta_{w,o} + a_1L_{\mathrm{LS}}\right] = 0 \tag{61}$$

Equations (60) and (61) can be solved for the length of the liquid sublayer, L_{LS}, and the wall temperature at the end of the sublayer, $\theta_{w,1}$.

In the dry region along the elongated bubble, equation (40) becomes:

$$\rho_w c_{\mathrm{pw}} \delta_w u_{\mathrm{LB}} \frac{\mathrm{d}T_w}{\mathrm{d}z} = q''_H - q''_{\mathrm{dry}} \tag{62}$$

where:

$$q''_{\mathrm{dry}} = H_v(T_w - T_{\mathrm{sat}}) \tag{63}$$

Equation (62) can be rewritten as:

$$\frac{\mathrm{d}\theta_w}{\mathrm{d}z} = a_1 - b_3\theta_w \tag{64}$$

where a_1 was defined before and $b_3 = H_v/(\rho_w c_{\mathrm{pw}} \delta_w u_{\mathrm{LB}})$.

The solution of equation (64) with the boundary condition given by equation (54) is:

$$\theta_w(z) = \theta_{w,1}\mathrm{Exp}[-b_3(z - L_{\mathrm{LS}})] + \frac{a_1}{b_3}\{1 - \mathrm{Exp}[-b_3(z - L_{\mathrm{LS}})]\} \tag{65}$$

In particular, equation (65) yields:

$$\theta_{w,2} = \theta_w(L_{\mathrm{LB}}) = \left(\theta_{w,1} - \frac{a_1}{b_3}\right)\mathrm{Exp}[-b_3(L_{\mathrm{LB}} - L_{\mathrm{LS}})] + \frac{a_1}{b_3} \tag{66}$$

The wall temperature distribution in the dispersed bubble region is obtained in a manner similar to that for case (A). Specifically, equation (55) can be replaced by:

$$\frac{\theta_w(z) - \vartheta_1}{\theta_w(z) - \vartheta_2} = \frac{\theta_{w2} - \vartheta_1}{\theta_{w2} - \vartheta_2}\mathrm{Exp}[-b_{22}(\vartheta_1 - \vartheta_2)(z - L_{\mathrm{LB}})] \tag{67}$$

Now, for a given $\delta_{\mathrm{LS,o}}$, the combined equations (65)-(67) can be readily solved for $\theta_{w,0}$, $\theta_{w,1}$ and $\theta_{w,2}$. Furthermore, substituting the calculated values back into equations (65) and (67), the wall temperature distributions along each subregion can be determined. Then, the average wall heat fluxes in the liquid sublayer and dry regions, respectively, can be obtained from:

$$\bar{q}''_{\mathrm{LS}} = \frac{k_l}{L_{\mathrm{LS}}}\int_0^{L_{\mathrm{LS}}} \frac{\theta_w(z)}{\delta_{\mathrm{LS}}(z)}\mathrm{d}z \tag{68}$$

$$\bar{q}''_{\mathrm{dry}} = \frac{H_v}{L_{\mathrm{LB}} - L_{\mathrm{LS}}}\int_{L_{\mathrm{LS}}}^{L_{\mathrm{LB}}} \theta_w(z)\mathrm{d}z \tag{69}$$

where $\delta_{\mathrm{LS}}(z)$ is given by equation (50). Also, the average wall heat flux in the nucleate boiling region is given by equation (58). The average wall temperature can still be obtained from equation (59).

In most practical cases, the equilibrium (or initial) thickness of the liquid sublayer is large enough, so that the heat transfer rate across the sublayer (mainly conduction) is smaller than the nucleate boiling heat transfer in the dispersed bubble region. If the elongated bubbles are short and/or the liquid film is thick, the liquid sublayer evaporates partially only, so that the liquid film extends along the entire bubble length. This situation corresponds to case (A) discussed before. For a fixed average heating rate, the reduction of heat removal rate across the liquid sublayer results in a local heat flux increase between the elongated bubbles. This increase becomes significant as the surface area fraction occupied by the elongated bubbles gradually increases due to small bubble coalescence. This, in turn, causes the wall temperature and thus the nucleation rate of dispersed bubbles, to increase. As a result, the increase in the volumetric fraction of dispersed bubbles along the channel accelerates, thus limiting the amount of liquid replenishing at the surface. Since, for most practical cases of forced-convection boiling, bubbles departing from the heated wall are small (0.001 m in diameter or less) their deformation from spherical shape is minimal and can be ignored. Thus, in order to maintain bubbles identity in the gradually shrinking (due to coalescence) region between the elongated bubbles, the bubble concentration must be below the critical value of about 0.74. As soon as the net bubble production exceeds this limit, the individual bubbles cannot be maintained any longer. The resultant vapor film formation will make it impossible for the liquid to approach the heated wall, and the liquid sublayer between the elongated bubbles and the wall will immediately evaporate. This, in turn, will cause temperature excursion (CHF).

If the liquid sublayer evaporation rate is high and/or the elongated bubbles are sufficiently long, the liquid sublayer may partially evaporate even though fresh liquid is still supplied via the nucleate boiling section (case (B)). Such partial dryout of the liquid sublayer results in a slight wall temperature increase. If fresh liquid can still flow toward the wall following dispersed bubble departure, this increase does not necessarily lead to a sudden wall temperature excursion, at least as long as the small bubble concentration is below the value limiting liquid replenishment. However, the formation of a dry region underneath the elongated bubbles substantial diminishes the heat transfer rate along the long bubbles, thus causing a faster formation of dispersed bubbles. Hence, the temperature excursion is practically inevitable.

The models discussed above was converted into closure laws for a three field (continuous liquid, small bubbles and elongated bubbles) multidimensional computational multiphase fluid dynamics (CMFD) model, and incorporated into the CFX code. The overall model was validated against the experimental results of Hino and Ueda (1985). Those experiments of reference were performed for R113 at a pressure of 147 kPa. The heated test section was a 0.357 m long and 0.018 m ID tube, with a centrally located heated rod, 0.008 m diameter. The outer tube wall was insulated, and there was an unheated section installed upstream of the annulus shaped heated section, allowing the flow to reach fully-developed conditions at the entrance to the heater.

The approach used in the analysis was to take the experimental values of the mass flux and inlet temperature corresponding to various experimental runs, and vary the heater power until the proposed model triggered a wall temperature excursion. Then, the corresponding value of the heating rate was compared to the actual experimental heater power at which CHF was observed to occur. Typical results are shown in Figures 8-10.

Figure 8 shows color contours of various local flow parameters. As can be seen, the results are, qualitatively speaking, similar to those discussed in Section 3.1. In particular, subcooled liquid is observed at the channel exit, with the subcooling varying from 12 K near the unheated wall to about 5 K near the heated wall. However, the void distribution is much more dramatic, and the void fraction near the heated wall locally exceeds 0.7.

The predicted radial distributions of fluid velocities and volume fractions are shown in Figure 9, and the axial distributions of the local heat flux in the dispersed bubble region and of the near-wall void fraction are shown in Figure 10. The velocities of liquid, of small dispersed bubbles and of the elongated bubbles flowing along the heated surface are presented there. As can be seen, the elongated bubbles flow faster than small bubbles (the effect of reduced drag); however, their presence accelerates small bubbles nucleating in the wall space available between the long bubbles.

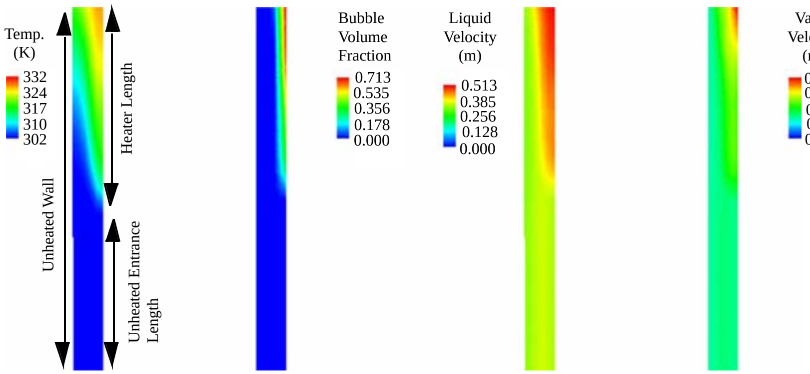

Figure 8.
Calculated temperature, void fraction and velocity contours in subcooled boiling: mass flux = 512 kg/m^{2}s, heat flux = 241 kW/m^2, inlet subcooling = 30 K

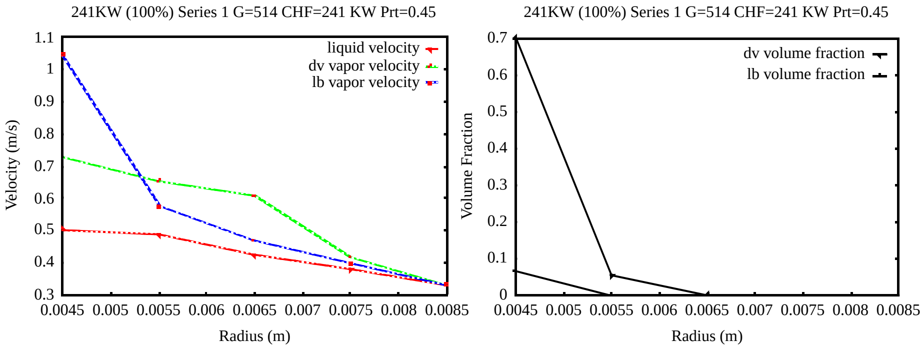

Figure 9.
Predicted radial velocity and void fraction distributions in subcooled boiling: mass flux = 512 kg/m^{2}s, heat flux = 241 kW/m^2, inlet subcooling = 30 K

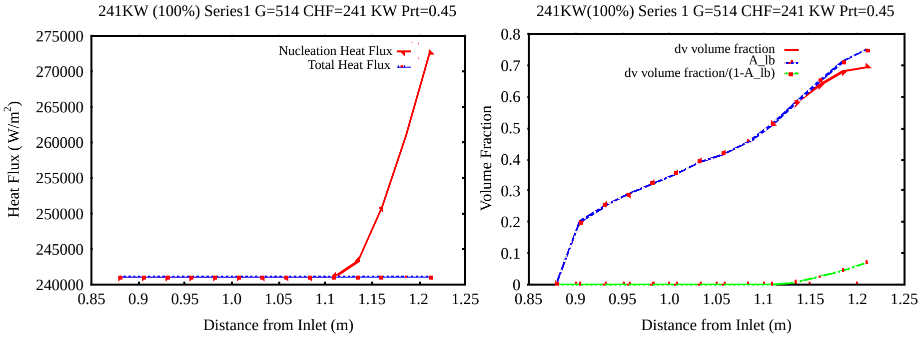

Figure 10.
Predicted axial distributions of the nucleate boiling heat flux and near-wall void fraction in subcooled boiling: mass flux = 512 kg/m^{2}s, heat flux = 241 kW/m^2, inlet subcooling = 30 K

It is interesting to notice that the higher vapor velocities also affect the liquid velocity profile, so that the maximum velocity is reached close to the heated wall. The fact that elongated bubbles flow only near the heated wall is also shown in Figure 9. Whereas their volume fraction near the wall may be relatively small, the overall impact of the elongated bubbles is actually quite strong. This is because the presence of those bubbles reduces the area fraction occupied by small bubbles, so that the actual concentration of small bubbles is augmented, as shown in Figure 10. In this particular case, the average volume fraction of small bubbles at the exit of 0.7 translates into the actual concentration of 0.75 in the nucleate boiling sections of the wall.

As can be seen from Figure 10, whereas the total wall heat flux is constant along the flow, the local heat flux in the dispersed bubble (nucleate boiling) region starts increasing beyond the average heating rate. This is because the heat transfer across the liquid film in the elongated bubble region is less effective. Consequently, in order to maintain the average constant heating rate, the local heat flux in the dispersed bubble region, and the corresponding wall temperature, must start increasing as the population of elongated bubbles grows along the flow (Figure 10). In the present case, the local wall heat flux near channel exit exceeds 270 kW/m^2, compared to the average heat flux of 241 kW/m^2.

The analysis of the results shows that the formation of elongated bubbles significantly accelerates the increase of local void fractions near the wall. Specifically, whereas the average void fraction of dispersed bubbles (per unit volume of the computational cell) does not exceed 0.7, the actual small bubble concentration between the elongated bubbles is about 0.75. Given the fact that the upper physical limit for the volume faction of spherical bubbles is 0.74, from this point on the dispersed bubbles will rapidly start coalescing, thus preventing liquid replenishment into the liquid sublayer between the elongated bubbles and the wall. This, in turn, will immediately trigger the wall temperature excursion. We conclude from the above that the assumed wall heat flux of 241 kW/m^2 is just beyond the onset of CHF. Converting the difference between the actual volume fraction value of 0.75 and the critical value of 0.74 into the corresponding power level difference, implies that the calculated onset of CHF occurred at about 238 kW/m^2.

It is important to note that the predictions agree well with the experimental data not only for the onset of CHF, but also for the wall temperature as well. The measured temperature of the heated surface at channel exit prior to the occurrence of CHF was 24.2 K, whereas the calculated temperature was about 23.5 K.

The results of this and other CFD simulations for selected sets of experimental conditions of Hino and Ueda (1985) are summarized in Table I.

As can seen from Table I, the agreement between the predictions and data are good, especially given the complexity of the problem and the discrepancies observed between

Case	Mass flux (kg/m^2 s)	Liquid subcooling (K)	Predicted CHF (kW)	Measured CHF (kW)	Error of CHF prediction (percent)	Predicted max. wall superheat	Measured max. wall superheat
1	512	30	238	241	2	25.5	24.2
2	512	20	172	211	16	20.8	23.1
3	1,236	30	305	332	8	24.8	26.9

Table I.
Predicted CHF results

experimental data from various sources. The prediction errors are small for high inlet subcooling cases, and slightly higher for lower subcooling and lower flow rate data. This is expected, since the intensity of boiling increases when either the inlet subcooling or mass flux decreases.

4. Importance of micro/nano scale phenomena

Predictions of boiling heat transfer in general, and CHF in particular, reported in the literature, are typically characterized by considerable inaccuracies. Possible explanations include reasons such as the inherent experimental uncertainties and the complex local multiphase flow patterns and modes of heat transfer. However, it also important to account for the possible effects of micro (or even nano) scale phenomena characterizing the solid-surface/liquid/gas interface on bubble size, shape and motion. In particular, the presence and properties of the liquid sublayer that separates the gas/vapor from the wall may have a considerable impact on the near-wall flow structure and heat transfer.

As an illustration, let us consider the geometry and flow conditions of long air bubbles in an inclined tube filled with distilled water are shown in Figure 11. The pipe geometry and material, and the bubble size, are identical in both cases. However, the bubble in Figure 11(a) is in direct contact with the wall, whereas the one in Figure 11(b) is separated from the wall by a thin liquid film. As a result of different shapes and wall shears, the bubble velocity was different for each case; specifically, the velocity of the bubble in Figure 9(b) was almost 20 percent higher. The only reason for that was that the result in Figure 9(a) was obtained for a clean surface of the tube (clearly, a non-wetting case), whereas in the other case the surface was coated with a tiny layer of nanoparticles which improved surface wettability and lead to liquid film formation between the bubble and the wall. Two interesting issues arise from Figure 11. First, if specific boiling experiments were performed for the same conditions, but using heaters characterized by different surface properties (such as wettability), the measured boiling heat transfer in general, and the CHF in particular, would likely experience some systematic differences. Secondly, if the surface is wetted, the question of liquid film thickness must be addressed to understand the underlying flow and heat transfer phenomena.

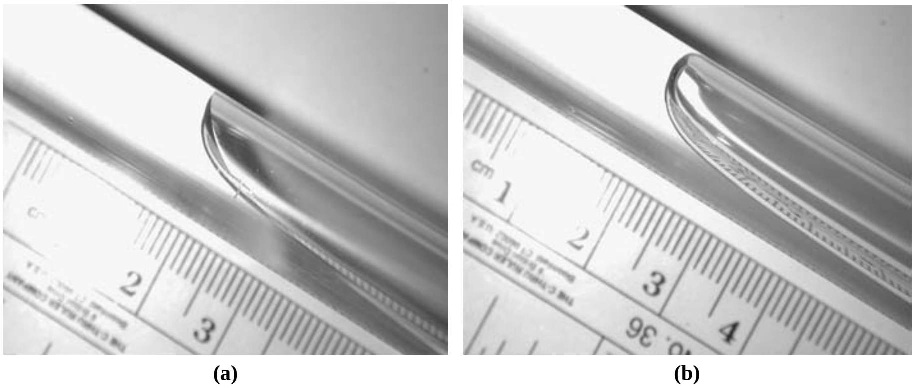

(a) **(b)**

Source: Podowski and Hirsa (2001)

Figure 11. The shape of air bubble tip in double-distilled water flowing along a 9 mm diameter inclined polycarbonate tube: (a) clean surface; (b) surface coated with minute amount of 38 nm alumina particles

The physics of thin and ultra-thin films formed along solid surfaces is concerned with the analysis of liquid spreading induced by surface motion. The issues of interest include the characteristics of the capillary region and the macroscopic contact angle, the development of ultra-thin (nanometer range) films by fully-wetting fluids, and thin-film evaporation. A primary question in the case of surface-motion-induced film coating is concerned with the effect of surface velocity on film thickness. This is shown in Figure 12.

It turns out that by using a rigorous approach to film fluid mechanics, a complete analytical multi-scale model can be derived, together with an efficient solution method (Podowski and Kumbaro, 2004). This model proves useful for explaining the effect of surface velocity on the liquid film thickness and, furthermore, shows the importance of accounting for velocity distribution across the film on film thickness predictions.

The motion of liquid film can be described by a unidirectional momentum equation along the surface:

$$\frac{\partial \tau_{yx}}{\partial y} = -\frac{\partial(\sigma K + \Phi)}{\partial x} + \rho g \tag{70}$$

where K is the surface curvature, $\Phi = B/\delta^{\mathrm{n}}$ represents the disjoining pressure at the liquid-vapor interface, δ is the film thickness, and the remaining notation is conventional.

A profound difficulty in solving equation (70) is due to the fact that the liquid film encompasses regions of dramatically different scales, from mm (in the initial capillary region) to nm (in the asymptotic region, where the van der Vaals forces are dominant). It turns out that a consistent and accurate solution to this problem can be obtained by introducing an intermediate region, where both the capillary and disjoining pressures are important. A typical solution for a stationary film, shown in Figure 13, clearly illustrates dramatic changes in film geometry between the capillary, transition and nano regions.

Solving equation (70) for the case of a moving wall shows that the film asymptotically reaches a constant thickness. However, an analysis of the solutions for various wall velocities indicates that, except for very small wall velocities (μm/s), the asymptotic film thickness along a moving surface is beyond the range of van der Vaals

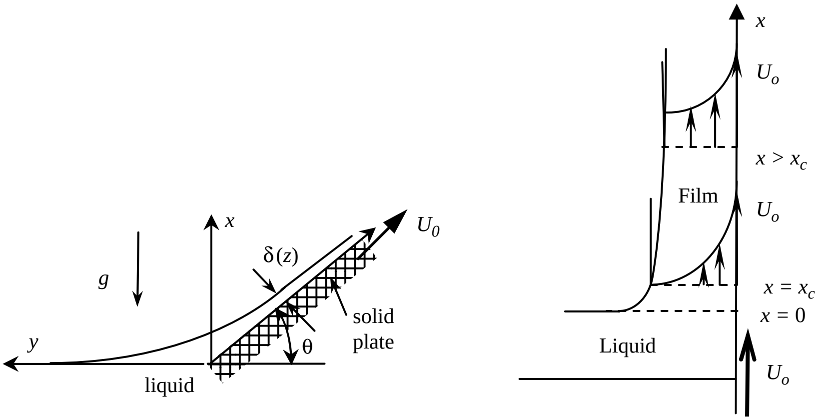

Figure 12.
Schematic of liquid film along a moving plate submerged in liquid pool: (a) liquid film along inclined moving wall; (b) development of film velocity

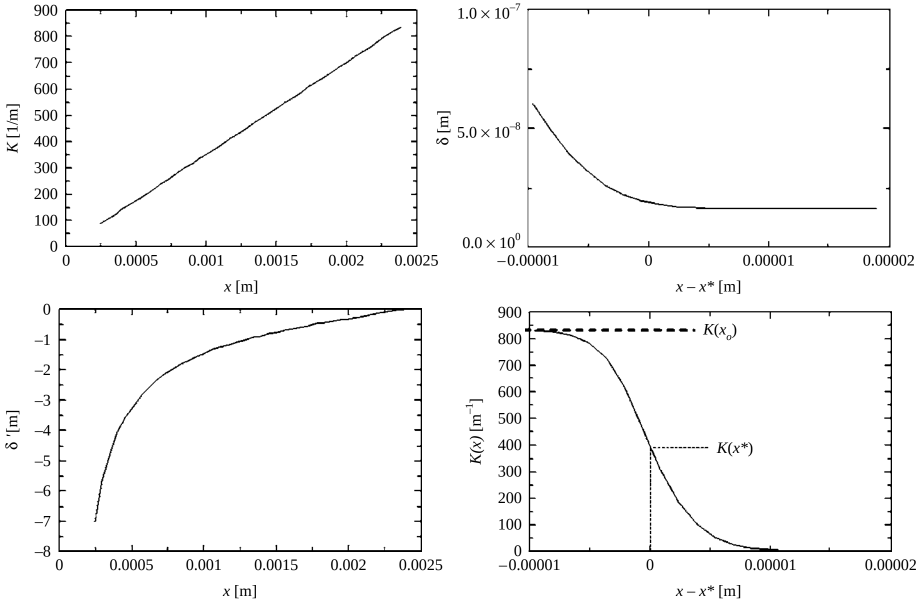

Figure 13. Liquid film characteristics on a vertical stationary wall: (a) meniscus region; (b) transition and nano regions

forces, and it stays in the micrometer rather than nano-meter range. This is shown in Figure 14(a).

Introducing the non-dimensional asymptotic film thickness and the capillary number, respectively, $\Delta = \delta_\infty \sqrt{\rho g/\sigma}$ and $\mathrm{Ca} = \mu U_0/\sigma$, the solution of the present model can be written as:

$$\Delta = 0.88(\mathrm{Ca})^{0.555} \tag{71}$$

Equation (71) is shown in Figure 14(b). A detailed derivation of the approach discussed above (Hino and Ueda, 1985) demonstrates that it can be used to: evaluate ultra-thin film thickness over the full range of surface inclination angles, from 0 to 90° deduce the Hamaker constant based on a single measured value of film thickness in the disjoining-pressure-controlled region, explain why the liquid film thickness on moving surfaces is normally beyond the range of van der Waals forces, and formulate a relationship between the asymptotic film thickness and the capillary number that accounts for the effect of gravity on film velocity for any surface inclination angle.

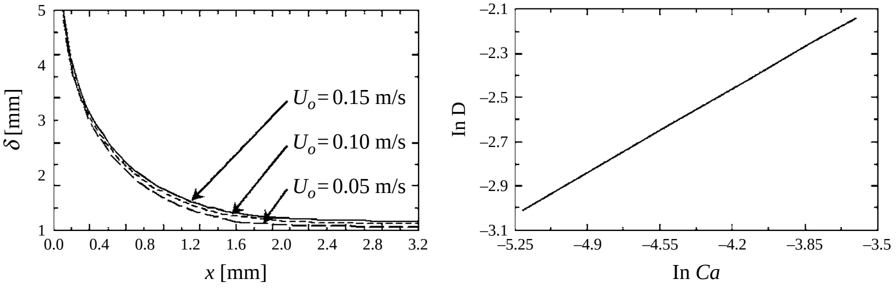

Figure 14. The effect of surface velocity on liquid film thickness: (a) film thickness for different wall velocities; (b) non-dimensional asymptotic film thickness vs capillary number

5. Conclusions

Several aspects of mechanistic multidimensional modeling and computer simulations of two-phase flows and heat transfer have been discussed. It has been shown that significant progress has recently been made in this field.

A complete multidimensional CMFD model of two-phase flow has been presented, including local constitutive models applicable to two-phase flows in heated channels. The physical modeling assumptions used in the proposed closure laws have been parametrically tested and validated against experimental data. It has been demonstrated that the overall model is capable of capturing various local flow and heat transfer phenomena in general, and the onset of temperature excursion (CHF) in low-quality forced-convection boiling, in particular.

References

AEA (1998), *CFX 4.2 Flow Solver User's Guide*, AEA Technology, Harwell.

Alajbegovic, A., Kurul, N., Podowski, M.Z., Drew, D.A. and Lahey, R.T. Jr (1996), "A CFD analysis of multidimensional flow phenomena in two-phase flow using a two-fluid model", *ANS Proc. 31st National Heat Transfer Conference, Houston, TX*, Vol. HTC 9.

Alajbegovic, A., Kurul, N., Podowski, M.Z., Drew, D. and Lahey, R.T. Jr (1997), "A new mechanistic model of critical heat flux in forced-convection subcooled boiling", *Proc. of the Eight International Topical Meeting on Nuclear Reactor Thermal-Hydraulics (NURETH-8), Kyoto, Japan*, pp. 973-80.

Anglart, H., Nylund, O., Kurul, N. and Podowski, M.Z. (1977), "CFD prediction of flow and phase distribution in fuel assemblies with spacers", *Nuclear Engineering and Design*, Vol. 177.

Antal, S.P., Ettorre, S., Kunz, R. and Podowski, M.Z. (2000), "Development of a next generation computer code for the prediction of multicomponent multiphase flows", *Proc. Int. Meeting on Trends in Numerical and Physical Modeling for Industrial Multiphase Flow, Cargese, France*.

Ceumern-Lindenstjerna, W.B.V. (1977), "Bubble departure diameter and release frequencies during nucleate pool boiling of water and aqueous NaCl solution", in Hahne, E. and Grigull, U. (Eds), *Heat Transfer in Boiling*, Academic Press and Hemisphere, New York, NY.

Del Valle, M. and Koening, D.B.R. (1985), "Subcooled flow boiling at high heat flux", *Int. J. Heat Mass Transfer*, Vol. 28, pp. 1907-20.

Drew, D.A. and Passman, S.L. (1999), *Theory of Multicomponent Fluids*, Springer-Verlag, New York, NY.

Galloway, J.E. and Mudawar, I. (1993), "CHF mechanism in flow boiling from a short heated wall – I. Examination of near-wall conditions with the aid of photomicrography and high-speed video imaging", *Int. J. Heat Mass Transfer*, Vol. 36, p. 36.

Gersey, C.O. and Mudawar, I. (1995), "Effects of heater length and orientation on the trigger mechanism for near-saturated flow boiling critical heat flux – I. Photographic study and statistical characterization of the near-wall interfacial features", *Int. J. Heat Mass Transfer*, Vol. 36.

Hino, R. and Ueda, T. (1985), "Studies on heat transfer and flow characteristics in subcooled flow boiling – Part 2. Flow characteristics", *Int. J. Multiphase Flow*, Vol. 11, pp. 283-97.

Kurul, N. and Podowski, M.Z. (1990), "Multidimensional effects in forced convection subcooled boiling", *Proc. 9th International Heat Transfer Conference, Jerusalem, Israel.*

Kurul, N. and Podowski, M.Z. (1991), “On the modeling of multidimensional effects in boiling channels”, *ANS Proc. 27th National Heat Transfer Conference, Minneapolis, MN.*

Kurul, N., Alajbegovic, A. and Podowski, M.Z. (1996), “Multiphase modeling in CFX 4”, *Proc. Int. CFX Users Conf., London, UK*.

Lemmert, M. and Chawla, J.M. (1977), “Influence of flow velocity on surface boiling heat transfer coefficient”, in Hahne, E. and Grigull, U. (Eds), *Heat Transfer in Boiling*, Academic Press and Hemisphere, New York, NY.

Podowski, M.Z. (2000), “Toward mechanistic multidimensional modeling of forced-convection boiling”, Boiling 2000: Phenomena and Emerging Applications, Girdwood.

Podowski, M.Z. (2007), “On the mechanistic modeling of interfacial phenomena in gas/liquid two-phase flows”, *Proc. 6th Int. Conference on Multiphase Flow, Leipzig, Germany*.

Podowski, M.Z. and Hirsa, A. (2001), “The effect of nanoparticles on Taylor-Bubble motion in inclined pipes”, paper presented at 4th Int. Conference on Multiphase Flow (ICMF), New Orleans, LA.

Podowski, M.Z. and Kumbaro, A. (2004), “The modeling of thin liquid films along inclined surfaces”, *Journal of Fluids Engineering*, Vol. 126, pp. 565-72.

Podowski, M.Z., Alajbegovic, A., Kurul, N., Drew, D.A. and Lahey, R.T. Jr (1997), “Mechanistic modeling of CHF in forced-convection subcooled boiling”, *ANS Proc. 32nd National Heat Transfer Conference, Baltimore, MD*, Vol. HTC-10.

Podowski, R.M., Drew, D.A., Lahey, R.T. Jr and Podowski, M.Z. (1997), “A mechanistic model of the ebullition cycle in forced-convection subcooled boiling”, *Proc. 8th International Topical Meeting on Nuclear Reactor Thermal-Hydraulics (NURETH-8), Kyoto, Japan*, pp. 1530-7.

Staub, F.W. (1968), “The void fraction in subcooled boiling – prediction of the initial point of net vapor generation”, *Journal of Heat Transfer*, Vol. 90, pp. 151-7.

Tiwari, P., Antal, S.P. and Podowski, M.Z. (2003), “On the modeling of dispersed particulate flows using a multifield model”, in Bathe, K.J. (Ed.), *Computational Fluid and Solid Mechanics*, Vol. 1, pp. 1160-5.

Tolubinsky, V.I. and Kostanchuk, D.M. (1970), “Vapour bubbles growth rate and heat transfer intensity at subcooled water boiling”, *Proc. 4th International Heat Transfer Conference*, Paper No B-2.8, Paris, France, Vol. 5.

Velidandla, V., Putta, S., Roy, R.P. and Kaira, S.P. (1995), “Velocity field in turbulent subcooled boiling flow”, *Proc. 30th National Heat Transfer Conference, Portland, OR*, Vol. HTD 314.

Corresponding author
Michael Z. Podowski can be contacted at: podowm@rpi.edu